Check for updates

Ultrathin, High Capacitance Capping Layers for Silicon Electronics with Conductive Interconnects in Flexible, Long-Lived Bioimplants

*Jinghua Li, Rui Li, Chia-Han Chiang, Yishan Zhong, Haixu Shen, Enming Song, Mackenna Hill, Sang Min Won, Ki Jun Yu, Janice Mihyun Baek, Yujin Lee, Jonathan Viventi, Yonggang Huang, and John A. Rogers**

Bioimplants that incorporate active electronic components at the tissue interface rely critically on materials that are biocompatible, impermeable to biofluids, and capable of intimate electrical coupling for high-quality, chronically stable operation in vivo. This study reports a materials strategy that combines silicon nanomembranes, thermally grown layers of SiO_2 and ultrathin capping structures in materials with high dielectric constants as the basis for flexible and implantable electronics with high performance capabilities in electrophysiological mapping. Accelerated soak tests at elevated temperatures and results of theoretical modeling indicate that appropriately designed capping layers can effectively limit biofluid penetration and dramatically extend the lifetimes of the underlying electronic materials when immersed in simulated biofluids. Demonstration of these approaches with actively multiplexed, amplified systems that incorporate more than 100 transistors in thin, flexible platforms highlights the key capabilities and the favorable scaling properties. These results offer an effective encapsulation approach for long-lived bioelectronic systems with broad potential for applications in biomedical research and clinical practice.

1. Introduction

A critical challenge in the development of flexible bioimplants is in the materials science and device engineering of chronically stable bioelectronic interfaces.[1–3] In some cases, the required timescales correspond to the lifespan of the patient, multiplied by some factor to provide an engineering margin of safety, thus reaching timescales that can reach hundreds of years. The most sophisticated types of bioimplants for neuroscience research and for envisioned classes of biomedical devices for human use involve active semiconductor functionality at the biointerface for multiplexing, local signal amplification, light emission/detection, and other functions with high spatiotemporal resolution across large areas.[4–9] This mode of operation involves electrical biases and continuous power supplied across the entire platform,

Dr. J. Li, H. Shen, Prof. J. A. Rogers
Department of Materials Science and Engineering
Northwestern University
Evanston, IL 60208, USA
E-mail: jrogers@northwestern.edu

Dr. J. Li, Y. Zhong, Dr. E. Song, Dr. S. M. Won, Prof. J. A. Rogers
Department of Materials Science and Engineering
Frederick Seitz Materials Research Laboratory
University of Illinois at Urbana-Champaign
Urbana, IL 61801, USA

Dr. J. Li
Department of Materials Science and Engineering
Center for Chronic Brain Injury
The Ohio State University
Columbus, OH 43210, USA

Prof. R. Li
State Key Laboratory of Structural Analysis for Industrial Equipment
Department of Engineering Mechanics
International Research Center for Computational Mechanics
Dalian University of Technology
Dalian 116024, P. R. China

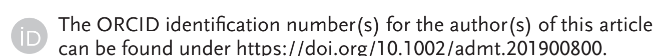
The ORCID identification number(s) for the author(s) of this article can be found under https://doi.org/10.1002/admt.201900800.

DOI: 10.1002/admt.201900800

C.-H. Chiang, M. Hill, Prof. J. Viventi
Department of Biomedical Engineering
Duke University
Durham, NC 27708, USA

Dr. E. Song, Dr. S. M. Won
Center for Bio-Integrated Electronics
Northwestern University
Evanston, IL 60208, USA

Prof. K. J. Yu
School of Electrical and Electronic Engineering
Yonsei University
Seoul 03722, Republic of Korea

J. M. Baek, Y. Lee
Department of Chemistry
University of Illinois at Urbana-Champaign
Urbana, IL 61801, USA

Prof. Y. Huang
Department of Civil and Environmental Engineering
Mechanical Engineering
Materials Science and Engineering
Center of Bio-Integrated electronics
Northwestern University
Evanston, IL 60208, USA

© 2019 WILEY-VCH Verlag GmbH & Co. KGaA, Weinheim

2365709x, 2020, 1, Downloaded from https://onlinelibrary.wiley.com/doi/10.1002/admt.201900800 by Sungkyunkwan University, Wiley Online Library on [14/04/2024]. See the Terms and Conditions (https://onlinelibrary.wiley.com/terms-and-conditions) on Wiley Online Library for rules of use; OA articles are governed by the applicable Creative Commons License

immediately adjacent to sensitive biological tissues. Here, a biocompatible measurement/stimulation interface serves also as a barrier against both biofluid penetration and current leakage, to avoid damage to the tissue and to the electronics.

An ideal engineered interface for this purpose should offer: 1) efficient coupling between the electronics and the body for high-fidelity sensing/actuation, 2) low reactivity in biofluids, and 3) perfect barrier properties for electrical and materials isolation from surrounding biofluids. Conventional encapsulation strategies that exploit deposited thin film coatings of organic and/or inorganic materials are effective for systems that consist of passive electrode arrays,[10–19] but typically fail to provide barrier function at a level required for powered electronics in advanced applications. Deficiencies arise from some combination of extrinsic (e.g., pinholes, grain boundaries, etc.) and intrinsic (e.g., permeability to water/ions, slow reactivity with biofluids, etc.) properties of the films.[20–23] The use of bulk materials in engineered containment enclosures can yield long lifetimes, but without the mechanical flexibility necessary to establish long-lived, intimate electronic interfaces to soft and fragile biotissues.[24–26]

Recent studies demonstrate that ultrathin layers of SiO_2 derived from growth on the surfaces of pristine, device-grade Si wafers through oxidation at high temperatures (1150 °C; thermal SiO_2 or t-SiO_2) can simultaneously serve as perfect barriers to biofluids and as capacitively coupled sensing interfaces, in high performance, flexible bioelectronics platforms with active semiconductor device functionality.[5,6] The relatively low dielectric constant (κ) of the t-SiO_2 and its small, but finite, rates of hydrolysis under aqueous conditions, however, set fundamental limitations in the scaling of the system. Specifically, to achieve sufficient capacitance coupling for sensing across the device platform, designs favor either large lateral dimensions for the measurement sites or reduced thickness for the t-SiO_2 layer. The former prevents high spatial resolution, while the latter limits the lifetimes set by hydrolysis.

As a solution, recent reports describe the use of heavily doped, patterned structures of p-type Si (p^{++}-Si) bonded intimately with layers of t-SiO_2, in structures that we denote as p^{++}-Si//t-SiO_2, for conductive vertical interconnect access (VIAs) that serve as arrays of electrically connections between the electronics and the surrounding biotissues.[27] Although this solution eliminates the constraints set by capacitive coupling, the hydrolysis rate of p^{++}-Si (0.5–100 nm d^{-1} at 37 °C)[27,28] is higher than that of t-SiO_2 (0.04–1.26 nm d^{-1} at 37 °C),[5,6,29] thereby limiting the lifetimes typically to several years, as determined by accelerated testing. Replacing the p^{++}-Si with $TiSi_2$ by reaction with Ti yields an insoluble alternative,[30] but additional studies of the properties of this silicide and its suitability as a chronic biointerface material are necessary. These circumstances motivate the continued development of alternative strategies.

Here we present materials designs and integration schemes for an approach that exploits a layer of HfO_2 formed by atomic layer deposition (ALD), a coating of Au deposited by thermal evaporation, and a structure of p^{++}-Si//t-SiO_2 to serve as a high capacitance sensing interface and chronically stable biofluid barrier for active, flexible electronic bioimplants. Experimental investigations and theoretical modeling results at elevated temperatures indicate that this materials system, at a total thickness of only ≈1 µm, can reach lifetimes of many decades, with favorable scaling properties to support high resolution mapping. The findings provide insights into the interface science and reactive diffusion mechanisms of silicon and metal oxide multilayer assemblies and suggest a realistic pathway for high-resolution and long-lived neural interfaces for chronic electrophysiology, with relevance to a wide range of applications in neuroscience and neuroengineering.

2. Results and Discussion

The fabrication focuses on formation of test platforms that include high-quality metal-oxide-semiconductor field-effect transistors (MOSFETs) and multilayer capping structures using adapted versions of otherwise standard semiconductor manufacturing techniques. **Figure 1** presents a schematic illustration of the sequence. Briefly, the process begins with a silicon-on-insulator (SOI) substrate with a 200 nm thick layer of device Si (p-type, concentration: 10^{17} cm^{-3}) and a 1 µm thick layer of buried oxide, t-SiO_2. Photolithographic patterning followed by wet/dry etching and thermal diffusion doping yields isolated nanomembranes (NMs) of n^{++}-Si (concentration: 10^{19} cm^{-3}) and p^{++}-Si (concentration: 10^{20} cm^{-3}) as the semiconductor material for the MOSFETs and the conductive material for VIAs to the biointerface, respectively (Figure 1A). Subsequent steps include deposition, patterning, and etching to form n-type MOSFETs with gate electrodes electrically connected to the patterned p^{++}-Si NMs, followed by casting of a uniform overcoat of polyimide (PI) (Figure 1B). A bonding process joins this PI to another thin sheet of PI on a temporary glass handle wafer using an adhesive layer and a coating of Al_2O_3 deposited by ALD. Reactive ion etching (RIE) then removes the Si wafer to expose the t-SiO_2 as the biofluid barrier (Figure 1C). Etching forms openings through the t-SiO_2 aligned to the p^{++}-Si NMs (Figure 1D). Thermal evaporation yields a thin layer of a noble metal (e.g., Au, Pt) on top of this p^{++}-Si//t-SiO_2 structure to define the sensing/stimulation sites and to reduce the rate of diffusion of water to the p^{++}-Si NMs. Treatment with O_2 plasma followed by conformal deposition of HfO_2 using ALD forms an ultrathin, high-κ dielectric layer as the basis of an insoluble capacitive biointerface that further reduces the rate of diffusion of water to the p^{++}-Si NMs. Peeling the device from the temporary glass substrate completes the fabrication. A layer of t-SiO_2 can be integrated onto the back side of the PI substrate to prevent biofluid penetration from this direction.[6]

Although many published reports describe the deposition of high-κ dielectrics (e.g., Al_2O_3, HfO_2) by ALD on noble

Prof. J. A. Rogers
Center for Bio-Integrated Electronics
Simpson Querrey Institute for BioNanotechnology
Department of Materials Science and Engineering
Biomedical Engineering
Chemistry
Mechanical Engineering
Electrical Engineering and Computer Science, and Neurological Surgery
McCormick School of Engineering and Feinberg School of Medicine
Northwestern University
Evanston, IL 60208, USA

 © 2019 WILEY-VCH Verlag GmbH & Co. KGaA, Weinheim

2365709x, 2020, 1, Downloaded from https://onlinelibrary.wiley.com/doi/10.1002/admt.201900800 by Sungkyunkwan University, Wiley Online Library on [14/04/2024]. See the Terms and Conditions (https://onlinelibrary.wiley.com/terms-and-conditions) on Wiley Online Library for rules of use; OA articles are governed by the applicable Creative Commons License

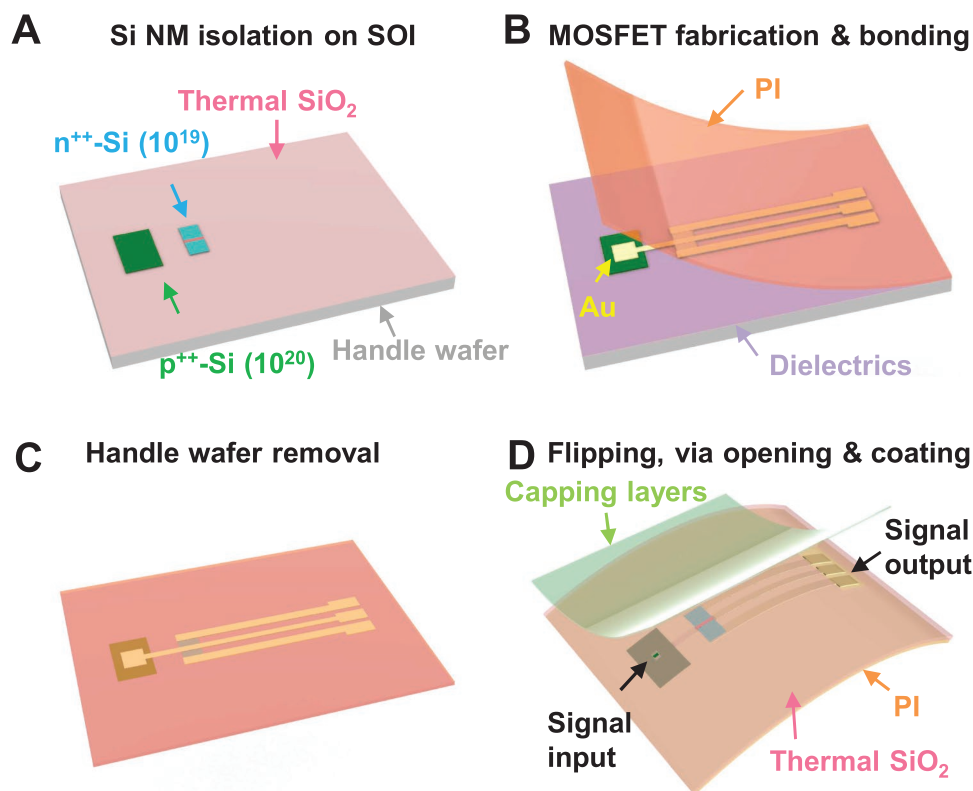

Figure 1. Schematic illustrations of integration strategies for use of a monolithic assembly of p^{++}-Si NM, t-SiO_2, and capping layers as sensing interfaces and biofluid barriers in flexible and long-lived biointegrated electronic systems. A) Doping and patterning of the device layer of an SOI substrate formed isolated p^{++}-Si and n^{++}-Si NMs on the buried oxide layer, t-SiO_2. B) Fabricating MOSFETs with gate electrodes electrically connected to p^{++}-Si NMs and encapsulating the device with PI on the top. C) Removing the Si handle wafer by dry etching to expose the bottom surface of the t-SiO_2. D) Flipping the device, opening small windows through the t-SiO_2 to locally expose the p^{++}-Si NMs as the electrical interconnects and then depositing capping layers to limit the penetration of biofluids and to form the biointerface.

metal surfaces (e.g., Au, Pt) for applications in energy storage, nano/microelectronics and other areas,[31–40] the underlying mechanisms are of interest due to the lack of naturally occurring hydroxyl groups on the surfaces of such metals. Formation of the initial growth interface during the ALD process can significantly affect the quality of the resulting films, of particular importance in demanding applications such those in biofluid barrier coatings. Measurements show that exposure to O_2 plasma enhances the hydrophilicity of the Au surface, and thus promotes the formation of the initial interface during the first several cycles of ALD. **Figure** 2A,B shows the water contact angle of thermally evaporated thin films of Au as a function of the O_2 plasma treatment time (0–120 s, power: 150 W) and corresponding photographs. Before the treatment, the Au surface is hydrophobic with a contact angle of ≈ 90°. The value drops to <10° after treatment for 1 min. X-ray photoelectron spectroscopy (XPS) reveals the surface conditions after O_2 plasma treatment for 5 min. The results plotted in Figure 2C,D show the relative peak intensities in the O 1s region. The untreated sample shows only a peak associated with adsorbed O (Figure 2C) while the treated one exhibits an additional peak from chemically bonded O (e.g., a stoichiometry of $AuO_{1.5}$ or Au_2O_3) (Figure 2D).[41] Previous reports describe the presence of hydroxyl groups as surface termination on transition metal oxides[42] and on Au via reactions between water and oxygen adatoms.[43] Proton transfer from water to this surface oxygen can yield surface-bound hydroxyl species that enhance the reactivity at the interface for the chemisorption of ALD precursors.[44,45] Evaporation of a layer of Ti or Cr,[46] or surface functionalization with self-assembled monolayer (e.g., by the use of OH-terminated alkanethiolate to form Au-S anchor on one end, and –OH groups on the other end for ALD growth)[47–49] can further improve the adhesion between the Au and HfO_2 and thus enhance the performance as a barrier material.

Systematic studies yield information on the biofluid barrier properties. For these experiments, a thin film of magnesium (Mg) deposited by electron-beam evaporation serves as a sensor for water penetration. Upon exposure to water, Mg quickly reacts to produce $Mg(OH)_2$ and H_2, and an associated dramatic change in optical properties, easily detectable by optical microscopy or visual inspection. **Figure** 3A shows an exploded view schematic illustration of such a Mg-based test device that includes a p^{++}-Si//t-SiO_2 structure with capping layers. The fabrication sequence follows steps outlined in Figure 1 but with photolithographically patterned islands of Mg in place of the MOSFETs. Reflectometry measurements reveal the dissolution behavior of films of p^{++}-Si and HfO_2 in aqueous solutions (20 mL) with chemical compositions relevant to biofluids (Figure 3B). At physiological temperatures (37 °C), the p^{++}-Si (sample size: 0.5 × 0.5 cm^2) decreases in thickness uniformly

 © 2019 WILEY-VCH Verlag GmbH & Co. KGaA, Weinheim

2365709x, 2020, 1, Downloaded from https://onlinelibrary.wiley.com/doi/10.1002/admt.201900800 by Sungkyunkwan University, Wiley Online Library on [14/04/2024]. See the Terms and Conditions (https://onlinelibrary.wiley.com/terms-and-conditions) on Wiley Online Library for rules of use; OA articles are governed by the applicable Creative Commons License

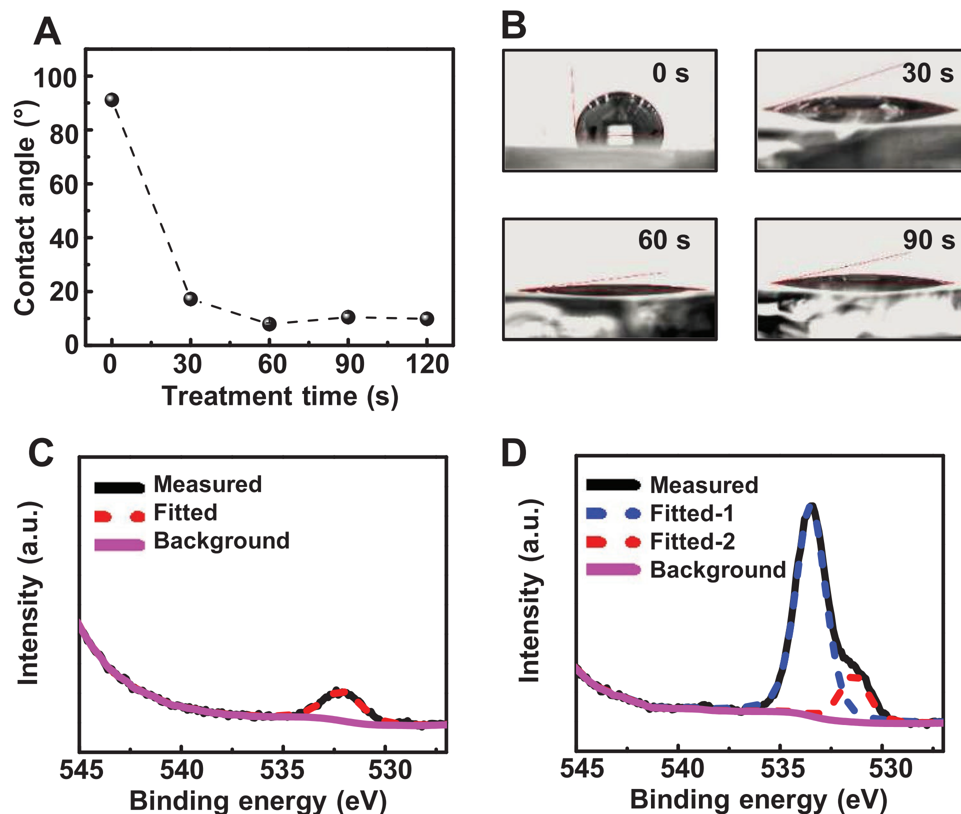

Figure 2. Surface characterization of Au before/after treatment with O_2 plasma. A) Water contact angle of the Au surface as a function of the O_2 plasma treatment time (0–120 s, pressure: 200 mTorr, power: 150 W). The Au film was exposed to air for 3 d after evaporation. The measurements occur immediately after treatment with O_2 plasma. B) Contact angle images of water droplets on Au surfaces with different treatment times. XPS spectra of Au surfaces C) before and D) after treatment with O_2 plasma (power = 150 W, pressure = 200 mtorr, treatment time = 5 min). The dashed lines represent fitted peaks of chemically bonded O and/or adsorbed O.

at a rate of ≈0.52 nm d^{-1} in phosphate buffered saline (PBS) and 0.56 nm d^{-1} in bovine serum through the reaction $Si + 4H_2O \rightarrow Si(OH)_4 + 2H_2$. By comparison, the thickness of the HfO_2 remains almost unchanged under similar conditions (Figure 3B) and even at elevated temperatures (96 °C) (Figure S1, Supporting Information). The results demonstrate that HfO_2 deposited by ALD is effectively insoluble in aqueous solutions with ions and/or proteins. Figure 3C shows a sequence of optical images of Mg pads beneath p^{++}-Si//t-SiO_2 structures without and with different capping layers. The areas in the images correspond to openings through the t-SiO_2 (1 µm) aligned to regions of p^{++}-Si (170 nm). Experiments at 96 °C on test structures without capping layers reveal average lifetimes of 2.65 d. After that, the Mg dissolves in a spatially uniform manner due to the complete hydrolysis of p^{++}-Si. Similar tests at different temperatures reveal average lifetimes of 10.7 and 20.2 d at 80 and 70 °C, respectively. These results are consistent with Arrhenius scaling where the lifetime depends exponentially on $1/T$ (Figure S2, Supporting Information).[6]

The addition of capping layers limits the diffusion of water to the p^{++}-Si and thereby reduces the rate of hydrolysis of this material. Specifically, a 300 nm thick capping layer of Au yields average lifetimes of 5.7, 20.4, and 50.1 d at 96, 80, and 70 °C. Figure S3 in the Supporting Information shows an optical image collected from the Au side before and after 5 d of immersion in PBS at 96 °C. The results indicate a stable interface between the Au and the Si with the formation of pinhole defects but no observable delamination. The coating of HfO_2 formed by ALD further extends the average lifetimes to 17.5, 63.4, and 154.2 d at 96, 80, and 70 °C, respectively. A summary of lifetimes for various capping layers are in Figure S4 in the Supporting Information. In all cases, the p^{++}-Si//t-SiO_2 structures serve as perfect, pinhole-free biofluid barriers while the capping layers reduce the rates of hydrolysis of the p^{++}-Si, as the main process that limits the lifetime. Devices with insoluble capping layers (Au and HfO_2) demonstrate a failure mode characteristic of water penetration through pinholes or other isolated defects, as forms of extrinsic factors reported in previous studies which is associated with the cleanroom environment available in academic research laboratory. Water that penetrates through such defects moves laterally over time due to diffusion along the interface, eventually dissolving the entire Mg pad. Figure S5 in the Supporting Information shows an example that highlights this behavior.

Accelerated soak tests in PBS using platforms that incorporate n-type MOSFETs (N-MOSFET, or NMOS) provide additional information on this multilayer encapsulation strategy. Here the thermal oxidation and doping steps partially consume the 200 nm thick Si NM on the SOI substrate to reduce its thickness to ≈60 nm. Figure 3D (inset) provides an optical

© 2019 WILEY-VCH Verlag GmbH & Co. KGaA, Weinheim

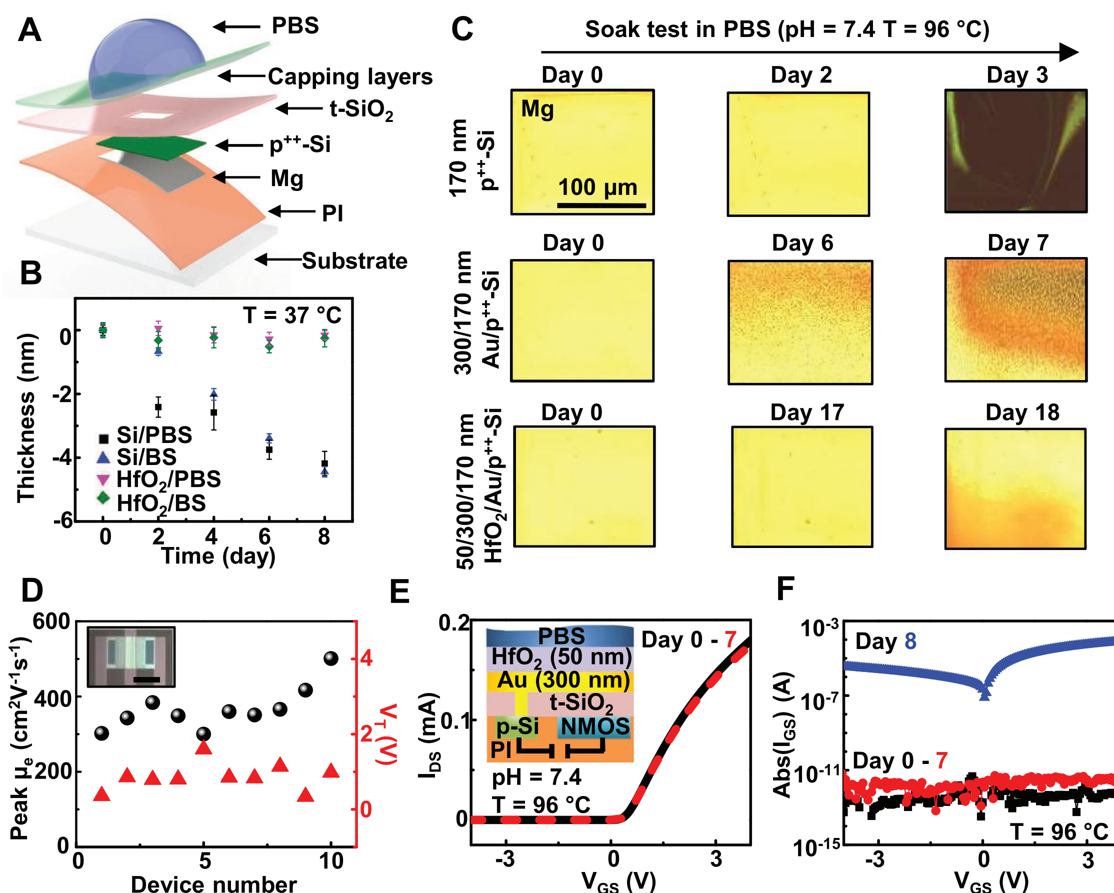

Figure 3. Effect of the types of capping layers on the lifetimes of passive and active devices. A) Exploded view schematic illustration of a Mg-based passive device used in soak tests. B) Measured changes in thickness as a function of time for layers of p^{++}-Si and HfO_2 immersed in PBS and bovine serum at 37 °C. C) Sequences of optical micrographs of Mg-based passive devices encapsulated by p^{++}-Si (170 nm)//t-SiO_2 (1 µm) without and with different capping layers (300 nm Au and 50 nm HfO_2) during immersion tests in PBS (pH = 7.4) at 96 °C. D) Statistics of threshold voltage and mobility of ten transistors produced in the manner described in Figure 1. Inset: Optical image of a transistor with channel length and width of 16 and 400 µm, respectively (scale bar: 200 µm). E) Transfer characteristics of a transistor with p^{++}-Si (60 nm)//SiO_2 (1 µm), Au (300 nm), and HfO_2 (50 nm) during a soak test at 96 °C in PBS (pH = 7.4). The device shows stable operation for 7 d. Inset: Cross-sectional view of the NMOS transistor used for the soak test, highlighting key functional layers. F) Leakage characteristics of the test transistor in frame (E) during immersion in PBS (pH = 7.4) at 96 °C. The results indicate catastrophic failure of the transistor at day 8.

image of an MOSFET with an effective channel length and width of 16 and 400 µm, respectively. The output characteristics in Figure S6 in the Supporting Information indicate expected performance, with Ohmic contacts. Figure 3D shows the statistics of the peak effective electron mobility and the threshold voltage of ten NMOS transistors prepared in this manner. Figure 3E presents the transfer characteristics of a representative transistor with a peak mobility of ≈300 $cm^2\ V^{-1}\ s^{-1}$ and a threshold voltage of ≈0.2 V. The inset shows a side-view schematic illustration of the test structure with capping layers (300 nm Au and 50 nm HfO_2). A representative device exhibits stable operation for ≈7 d at 96 °C in PBS (pH = 7.4), followed by a sudden increase in leakage current (Figure 3F). The findings are consistent with results obtained using Mg-based passive devices (with 170 nm p^{++}-Si) as described in the previous section. By comparison to previously reported lifetimes of Si biointerfaces,[27,28,30] the results presented here represent an improvement by a factor of ≈5–6.

Figure 4 illustrates a theoretical model of reactive diffusion for dissolution of the p^{++}-Si NM without and with capping layers of Au or HfO_2/Au. For the ultrathin multilayers under consideration, the initial thicknesses are sufficiently small compared to the in-plane dimensions such that 1D models can capture the diffusion and dissolution behaviors.[50] The water diffusivity in p^{++}-Si, D_{Si}, and the reaction rate constant between water and p^{++}-Si, k_{Si}, are key parameters for reactive diffusion modeling, for which a single layer model of p^{++}-Si with an initial thickness h_{Si} immersed in PBS is established in Figure 4A. Here, the z-axis lies along the thickness direction, with the origin O located at the bottom. The governing equation is $D_{Si}\partial^2 w/\partial z^2 - k_{Si} w = \partial w/\partial t\ (0 \le z \le h_{Si})$,[51] where w is the water concentration, which depends on both location z and time t. With a constant water concentration, w_0, of 1 g cm^{-3} at the top and zero water flux at the bottom surface of the p^{++}-Si layer, the boundary conditions are $w|_{z=h_{Si}} = w_0$ and $\partial w/\partial z|_{z=0} = 0$. The initial condition of zero water concentration throughout

© 2019 WILEY-VCH Verlag GmbH & Co. KGaA, Weinheim

2365709x, 2020, 1, Downloaded from https://onlinelibrary.wiley.com/doi/10.1002/admt.201900800 by Sungkyunkwan University, Wiley Online Library on [14/04/2024]. See the Terms and Conditions (https://onlinelibrary.wiley.com/terms-and-conditions) on Wiley Online Library for rules of use; OA articles are governed by the applicable Creative Commons License

2365709x, 2020, 1, Downloaded from https://onlinelibrary.wiley.com/doi/10.1002/admt.201900800 by Sungkyunkwan University, Wiley Online Library on [14/04/2024]. See the Terms and Conditions (https://onlinelibrary.wiley.com/terms-and-conditions) on Wiley Online Library for rules of use; OA articles are governed by the applicable Creative Commons License

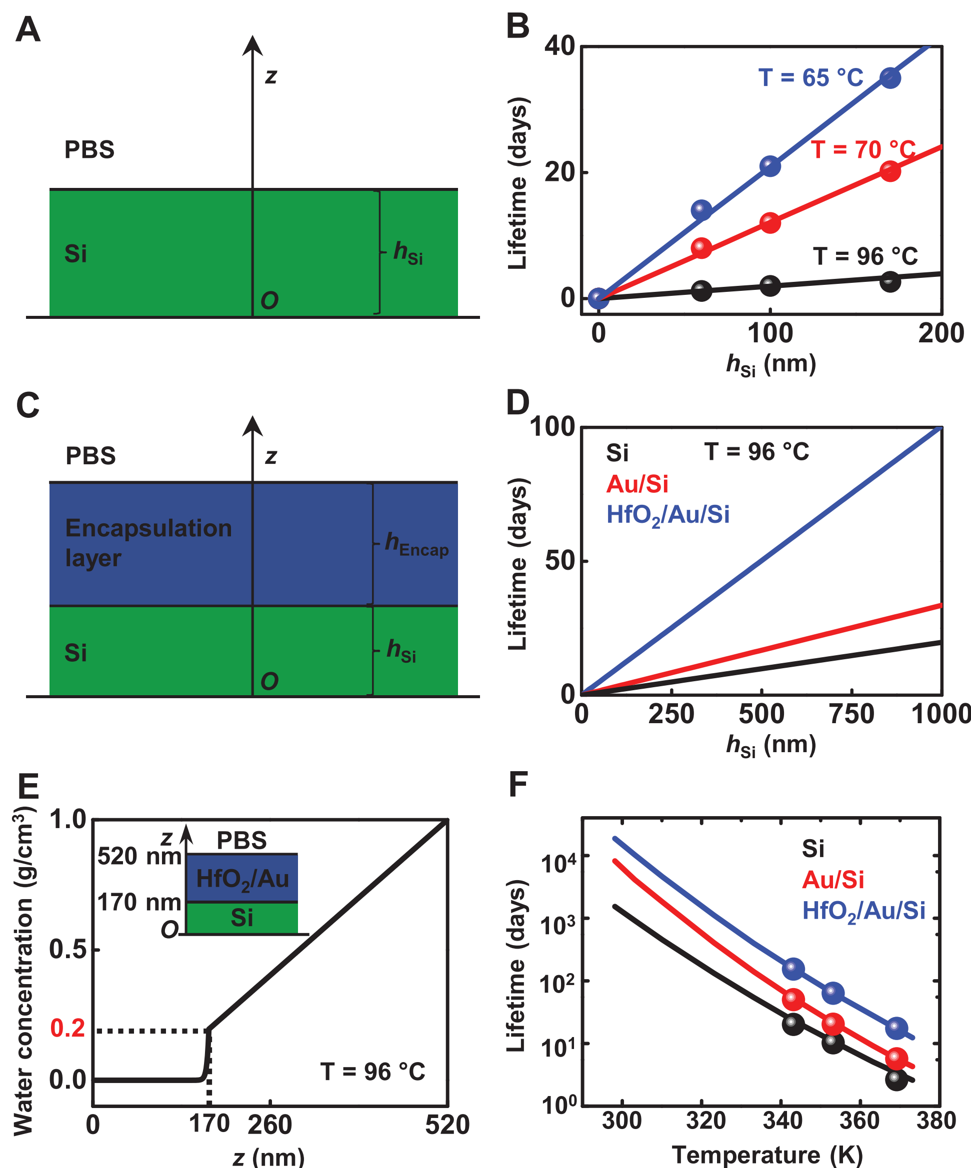

Figure 4. Theoretical modeling of reactive diffusion of p++-Si with Au or Au/HfO_2 capping layers. A) Schematic illustration of the single layer model. B) Theoretical (lines) and measured (dots) lifetimes of p++-Si as a function of initial thickness immersed in water at 65, 70, and 96 °C. C) Schematic illustration of the bilayer model. D) lifetimes of p++-Si without and with capping layer(s) as a function of initial p++-Si thickness immersed in water at 96 °C (HfO_2: 50 nm, Au: 300 nm). E) Distribution of saturated water concentration in a 50/300/170 nm thick HfO_2/Au/p++-Si structure immersed in water at 96 °C. F) Theoretical (lines) and measured (dots) temperature-dependent lifetimes of the p++-Si, Au/p++-Si, and HfO_2/Au/p++-Si structures immersed in water at 96 °C, with the thicknesses of HfO_2, Au, and p++-Si equal to 50, 300, and 170 nm.

the thickness requires $w|_{t=0} = 0$ $(0 \leq z < h_{Si})$. The variable separation method yields an analytic solution for w, by which the thickness of the dissolved p++-Si, $h_{dissolved}$, follows from integration of $h_{Si}M_{Si}k_{Si}w/(4\rho_{Si}M_{H_2O})$ over both z and t according to $Si + 4H_2O \rightarrow Si(OH)_4 + 2H_2$,[27] giving $h_{dissolved} \approx \left[M_{Si}w_0\sqrt{k_{Si}D_{Si}}\tanh\sqrt{k_{Si}h_{Si}^2/D_{Si}}/(4\rho_{Si}M_{H_2O})\right]t$ after omitting an infinite series summation that is negligible in this study (details appear in the Appendix, Supporting Information). Here, ρ_{Si} is the mass density of p++-Si (= 2.33 g cm^{-3}), M_{Si} (= 28 g mol^{-1}), and M_{H_2O} (= 18 g mol^{-1}) are the molar masses of p++-Si and water, respectively. Equating $h_{dissolved}$ with h_{Si}, the total time to reach full dissolution, i.e., the lifetime of the p++-Si layer, t_{life}, can be written as

$$t_{life} \approx \frac{6h_{Si}}{\sqrt{k_{Si}D_{Si}}\tanh\sqrt{\frac{k_{Si}h_{Si}^2}{D_{Si}}}} \quad (1)$$

With experimentally measured lifetimes for a 100 nm thick layer of p++-Si at 65 and 96 °C (21 and 2 d, respectively), D_{Si} and k_{Si} at different temperatures can be determined by applying the above model as $D_{Si} = 10^{-4.86-4121/T}$ cm^2 s^{-1} and $k_{Si} = 2.03 \times 10^8 \times e^{-9515/T}$ s^{-1} (T is the absolute temperature),

© 2019 WILEY-VCH Verlag GmbH & Co. KGaA, Weinheim

which follow Arrhenius scaling with an activation energy of 0.82 eV.[27] Figure 4B plots the lifetimes of a single layer of p^{++}-Si at three different temperatures (65, 70, and 96 °C) versus the initial thickness. The results from theoretical modeling (lines) agree well with experimental results (dots).

A bilayer model can describe the dissolution of p^{++}-Si with Au or HfO_2/Au capping layers (Figure 4C). For p^{++}-Si, the governing equation of the single layer model as well as the boundary condition $\partial w/\partial z|_{z=0} = 0$ and initial condition $w|_{t=0} = 0$ remain valid. Since both Au and HfO_2 do not react with water, as revealed by invariant thicknesses of thin films of these materials during soak tests, the behavior of water in Au or HfO_2/Au can be described by diffusion via extrinsic effects, without reaction, i.e., $D_{encap}\partial^2 w/\partial z^2 = \partial w/\partial t$ ($h_{Si} \le z \le h_{Si} + h_{encap}$), with the boundary condition $w|_{z=h_{Si}+h_{encap}} = w_0$ and initial condition $w|_{t=0} = 0$ ($h_{Si} \le z \le h_{Si} + h_{encap}$), where h_{encap} is the encapsulation thickness, and D_{encap} the effective water diffusivity in the capping layers, i.e., D_{Au} for Au or D_{equiv} for an equivalent layer of HfO_2/Au. The continuity of interfacial water concentration and flux requires $w|_{z=h_{Si}-0} = w|_{z=h_{Si}+0}$ and $D_{Si}\,\partial w/\partial z|_{z=h_{Si}-0} = D_{encap}\,\partial w/\partial z|_{z=h_{Si}+0}$. The variable separation method yields an analytic solution for the water concentration in the bilayer. Following the logic for the single layer model, the total time for full dissolution of the p^{++}-Si, i.e., the lifetime of the bilayer, t'_{life}, is

$$t'_{life} \approx \left(1 + \frac{h_{encap}\sqrt{k_{Si}D_{Si}}}{D_{encap}} \tanh\sqrt{\frac{k_{Si}h_{Si}^2}{D_{Si}}}\right) t_{life} \quad (2)$$

With D_{Si} and k_{Si} obtained from the single layer model and the experimentally measured lifetimes for the 300/170 nm thick Au/p^{++}-Si bilayer at 70 and 96 °C (50.1 and 5.7 d, respectively), D_{Au} at different temperatures can be determined by the bilayer model as $D_{Au} = 10^{0.65\,-\,5344/T}$ cm^2 s^{-1} based on the Arrhenius scaling. Similarly, soak tests for a 50/300/170 nm thick HfO_2/Au/p^{++}-Si structure give lifetimes of 154.2 and 17.5 d at 70 and 96 °C, respectively, which determine the equivalent water diffusivity in the 350 nm thick capping layer (HfO_2/Au) as $D_{equiv} = 10^{-1.51\,-\,4803/T}$ cm^2 s^{-1}.

Figure 4D plots the predictions of the lifetimes for three structures (p^{++}-Si, Au/p^{++}-Si, and HfO_2/Au/p^{++}-Si) at 96 °C versus the initial thickness of the p^{++}-Si, where the thicknesses of HfO_2 and Au are 50 and 300 nm, respectively. The lifetimes show an approximately linear dependence on h_{Si}. The distribution of saturated water concentration in a representative 50/300/170 nm thick HfO_2/Au/p^{++}-Si structure at 96 °C is shown in Figure 4E following the steady-state limit that is expressed in normalized form by

$$\frac{w_{saturation}}{w_0} = \begin{cases} \dfrac{\cosh\left(\sqrt{\dfrac{k_{Si}}{D_{Si}}}z\right)}{\cosh\sqrt{\dfrac{k_{Si}h_{Si}^2}{D_{Si}}} + \dfrac{h_{encap}\sqrt{k_{Si}D_{Si}}}{D_{equiv}}\sinh\sqrt{\dfrac{k_{Si}h_{Si}^2}{D_{Si}}}}, & 0 \le z \le h_{Si} \\[2ex] 1 - \dfrac{h_{Si} + h_{encap} - z}{h_{encap} + \dfrac{D_{equiv}}{\sqrt{k_{Si}D_{Si}}}\coth\sqrt{\dfrac{k_{Si}h_{Si}^2}{D_{Si}}}}, & h_{Si} \le z \le h_{Si} + h_{encap} \end{cases} \quad (3)$$

The modeling details appear in the Appendix in the Supporting Information. The results suggest that the water concentration is significantly reduced by the presence of the HfO_2/Au, reaching only 0.2 g cm^{-3} at the interface between these capping layers and the p^{++}-Si even after saturation. A dramatic decrease of water concentration to zero immediately under the top of p^{++}-Si indicates a surface-reaction-dominated kinetics for dissolution of p^{++}-Si in water. The theoretical temperature-dependent lifetimes of the three structures are in Figure 4F, where the 50/300 nm thick HfO_2/Au structure provides an increase in lifetime by an order of magnitude for the case of a 170 nm thick layer of p^{++}-Si. This lifetime is two times longer than that of an otherwise similar system but with a capping layer of only a 300 nm thick film of Au. The theoretical results (lines) are in good agreement with the experimental measurements conducted at high temperatures (dots) and are especially useful for low-temperature (e.g., body-temperature) lifetime predictions for chronic implantable devices that may live for decades,[30] where experimental studies are impractical. The extrapolated lifetimes at 37 °C of the three cases studies here are 451 (170 nm p^{++}-Si), 1811 (300 nm Au/ 170 nm p^{++}-Si), and 4574 (50 nm HfO_2/300 nm Au/ 170 nm p^{++}-Si) d.

These findings motivate the use of capping layers with the p^{++}-Si//SiO_2 structure as a biofluid barrier and sensing/stimulation biointerface for actively multiplexed, flexible Si electronics. **Figure 5**A compares the designs of arrays of Si MOSFETs for electrophysiology with different coupling strategies to biotissues. In the most basic design, a uniform layer of t-SiO_2 serves simultaneously as a barrier that prevents water penetration and a dielectric that capacitively couples the underlying semiconducting channels of the electronics to the surrounding biology.[5,6] As highlighted in the Introduction, the relatively low dielectric constant of t-SiO_2 and its slow reaction with water results in a tradeoff between lifetime, resolution, and interface coupling strength.[5] Conductive VIAs of p^{++}-Si through the t-SiO_2 address the limitation in electrical coupling by replacing the capacitive interface with a conductive one, but with increased rates of reaction with water. In the scheme introduced here, a metal pad and ultrathin layer of HfO_2 on top of the p^{++}-Si serves to slow the rates of water penetration and to form a direct, high capacitance contact to biotissues on one side, through the p^{++}-Si features, and conductive connection to the associated electronics on the other side.

Figure 5B shows an exploded view schematic illustration of this design. Each unit cell contains two Si MOSFETs: one to support multiplexed addressing and the other to buffer and amplify the signals. Photographs of a representative device with an interconnected array of 64 such unit cells before and after (inset) coating with a thermally evaporated layer of Au appear in Figure 5C. Figure 5D presents corresponding optical images of a unit cell with the via opening size of 30 × 30 μm^2 (channel length: 16 μm, channel width: 80 μm, p^{++}-Si: 270 × 190 μm^2, unit area: 360 × 360 μm^2). Additional optical images at key steps of the fabrication sequence appear in Figure S7 in the Supporting Information. Figure S8 in the Supporting Information presents the transfer characteristics of a test transistor with a similar layout, showing an on/off ratio of ≈10^6, a peak mobility of ≈400 cm^2 V^{-1} s^{-1} and a threshold voltage of ≈0.1 V.

© 2019 WILEY-VCH Verlag GmbH & Co. KGaA, Weinheim
2365709x, 2020, 1, Downloaded from https://onlinelibrary.wiley.com/doi/10.1002/admt.201900800 by Sungkyunkwan University, Wiley Online Library on [14/04/2024]. See the Terms and Conditions (https://onlinelibrary.wiley.com/terms-and-conditions) on Wiley Online Library for rules of use; OA articles are governed by the applicable Creative Commons License

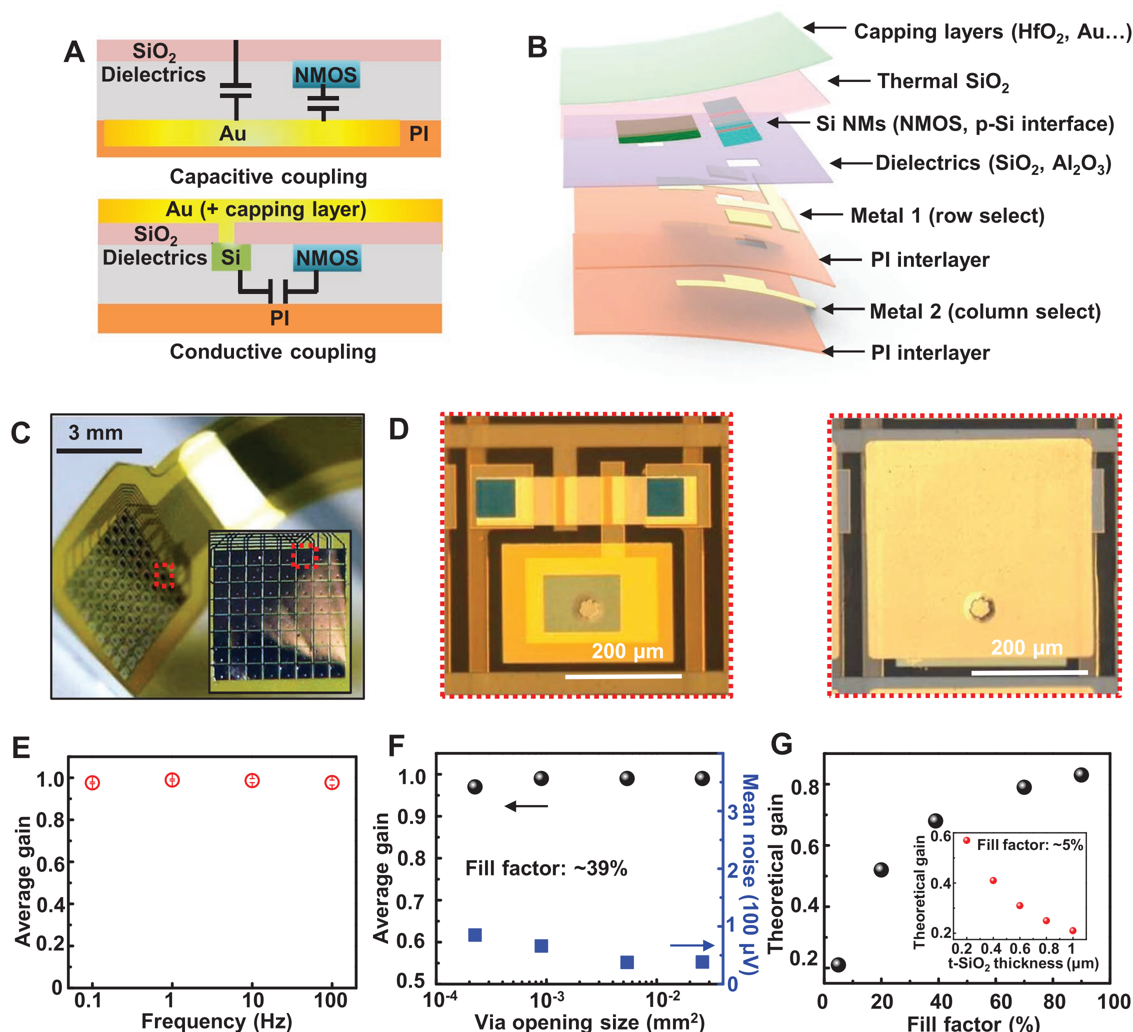

Figure 5. Comparisons between actively multiplexed Si electronics with capacitively and conductively coupled interface designs. A) Side-view schematic illustrations of electronics with t-SiO_2 (top) and capping layers/p^{++}-Si//t-SiO_2 (bottom) as the interface between the devices and the surrounding biology. B) Exploded view schematic illustration of the layer configuration for a system with capping layer(s)/p^{++}-Si//t-SiO_2. The labels highlight key functional layers. C) Photograph of a flexible sensing system with 128 transistors and an p^{++}-Si//SiO_2 interface in a slightly bent configuration. Inset: The device with capping layer (Au) on the top to define the sensing area and enhance the lifetime. D) Optical images of a sensing node before (left) and after (right) the deposition of metal on p^{++}-Si//SiO_2. E) Average gain of a representative device with 64 conductively coupled unit cells as a function of the input frequency (from 0.1 to 100 Hz). F) Average gain and mean noise as a function of via opening size for active electronics with conductively coupled designs (p^{++}-Si region: 270 × 190 µm^2, fill factor of p^{++}-Si: ≈39%, via opening size (from left to right): 15 × 15, 30 × 30, 60 × 90, and 200 × 130 µm^2). G) Theoretical gain values as a function of p^{++}-Si fill factor (1 µm t-SiO_2) and the thickness of t-SiO_2 (inset, p^{++}-Si fill factor: 5%) for capacitive coupling through t-SiO_2 interface.

In vitro assessments highlight the advantages of this design over capacitively coupled systems with a similar structure but without the conductive VIAs. The evaluations involve immersing the device into electrically biased PBS and collecting data with a back-end data acquisition system described in refs. [5, 6], and [27]. Figure 5E shows the average gain (defined as the ratio of output voltage to input voltage) of the 64 unit cells in a representative device as a function of the input frequency (0.1–100 Hz, input voltage: 2 mV). The performance is stable over a wide dynamic range with the average gain value of ≈0.99 (close to the design point of 1). Systematic studies reveal the effects of key parameters on the scalability of conductively coupled Si electronics for high resolution biopotential recording. Figure 5F displays the average gain and mean noise levels of a system as a function of via opening size in devices with a p^{++}-Si fill factor (defined as the ratio of p^{++}-Si region to the whole area of the unit) of 39%. The via dimensions range from 200 × 130 to 90 × 60, 30 × 30 and 15 × 15 µm^2, as displayed in Figure 5D and Figure S9 in the Supporting Information. In all cases, the devices with direct electrical coupling between PBS and the gate electrode of the transistors show stable performances with average gain and mean per-channel noise above 0.97 and below 85 µV, respectively. The ultimate dimension of the via opening is only limited by the features size than can be achieved by

© 2019 WILEY-VCH Verlag GmbH & Co. KGaA, Weinheim

2365709x, 2020, 1, Downloaded from https://onlinelibrary.wiley.com/doi/10.1002/admt.201900800 by Sungkyunkwan University, Wiley Online Library on [14/04/2024]. See the Terms and Conditions (https://onlinelibrary.wiley.com/terms-and-conditions) on Wiley Online Library for rules of use; OA articles are governed by the applicable Creative Commons License

lithographic patterning and etching. Minimizing the size of the p^{++}-Si enables further scaling. Figure 5G shows the theoretical gain value as a function of the fill factor with capacitive coupling through the t-SiO_2 (1 µm). The capacitance can be calculated using the following equation

$$C = \frac{\varepsilon_r \varepsilon_0 A}{t} \tag{4}$$

where ε_r is the relative permittivity, ε_0 is the vacuum permittivity, A is the area of the capacitor, and t is the thickness of the dielectric. For the capacitance of top-gate dielectrics (C_{TG}), $A = 16 \times 80$ µm^2, ε_r (t-SiO_2) = 3.9, t (t-SiO_2) = 50 nm, ε_r (Al_2O_3) = 11, t (Al_2O_3) = 13 nm. As an example, for the capacitance of the sensing interface (C_{CAP}) in a device with a fill factor of 5%, $A = 360 \times 360$ µm$^2 \times 5\%$, t (t-SiO_2) = 1 µm. Accordingly, $C_{CAP} \approx 0.3\ C_{TG}$. The total capacitance (C_T) driving the channel of the transistor in the buffer/amplifier can be calculated by combing C_{CAP} and C_{TG} in series

$$\frac{1}{C_T} = \frac{1}{C_{CAP}} + \frac{1}{C_{TG}} \tag{5}$$

which yields $C_T \approx 0.2\ C_{TG}$. As a result, the theoretical value of the gain is ≈0.2, as the sensing interface and the top gate dielectrics in series form a voltage divider structure. Similarly, a fill factor of ≈90% corresponds to a gain value of ≈0.83. The actual value might be slightly higher resulting from the effect of active shielding circuits in the acquisition electronics. Figure 5G (inset) highlights the theoretical gain as a function of the thickness of t-SiO_2 (p^{++}-Si fill factor: 5%), suggesting that the reduction of the thickness of the interface to 200 nm can yield a gain of ≈0.58. Therefore, there is a design trade-off between signal quality and device lifetime.

Capping layers of metal and high-κ dielectrics on top of the conductively coupled system forms an interface with much higher capacitance than that afforded by t-SiO_2 at thicknesses needed for chronic stability. The equivalent circuit diagram of a unit cell appears in Figure S10 in the Supporting Information. For HfO_2, $\varepsilon_r = 25$. With the high fill factor of Au of ≈100% (360 × 360 µm^2), the capacitance of 50 nm HfO_2 sensing interface $C_{CAP} \approx 700\ C_{TG}$. As a result, C_T is almost the same as C_{TG} according to Equation (5). More importantly, for the design that requires higher resolution with a smaller unit size and a minimized area of p^{++}-Si region, this design shows advantage over counterparts with t-SiO_2 interface.[27] For example, with a whole unit area as small as 80 × 80 µm^2, this design can provide a gain of 0.97.

Figure 6A shows the output characteristics of an amplifier in one sensing node in a device of this type with an alternating current (AC) signal of 20 mV (10 Hz, sine wave input). Figure 6B displays the histograms of gain values from 36 units in a typical system. The results indicate an average gain of 0.96. The mean per-channel noise is ≈25 µV (Figure 6C), suggesting no degradation in electrical performance compared to devices without an HfO_2 capping layer, as described in Figure 5 due

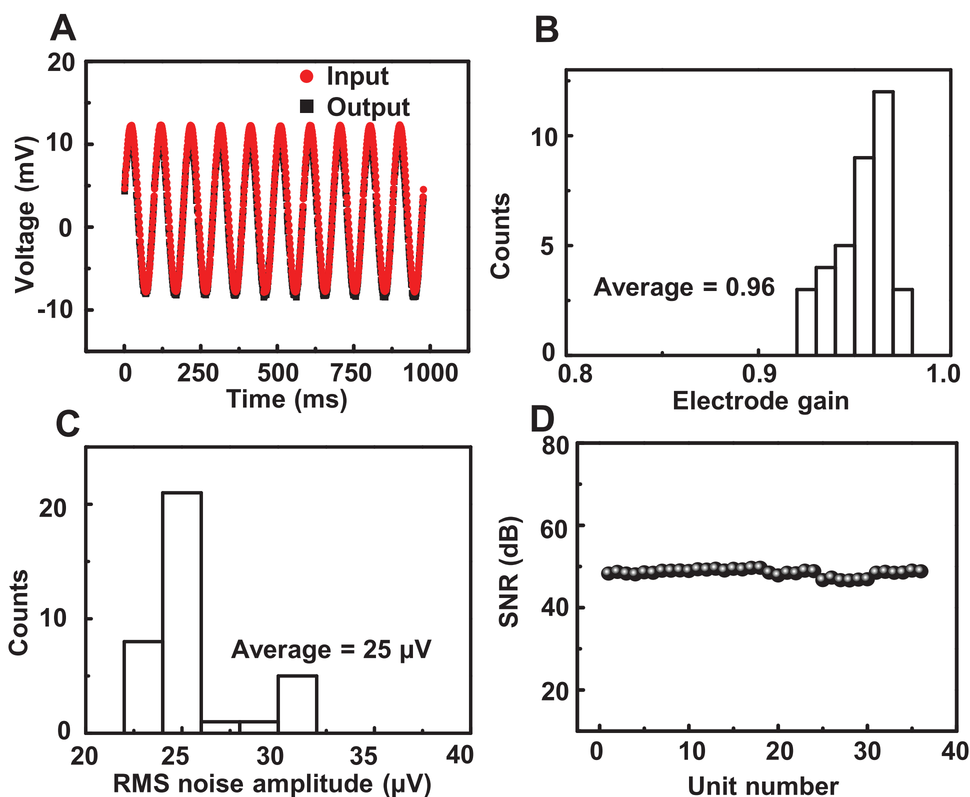

Figure 6. In vitro characterization of the electrical performance of a conductively coupled sensing system with Au (300 nm) and HfO_2 (50 nm) capping layers. A) Output characteristics of a sensing node with an AC input sine wave signal (20 mV, 10 Hz). B–D) Histograms of gain and noise, and statistics of signal-to-noise ratio associated with 36 sensing units in a typical device of this type.

© 2019 WILEY-VCH Verlag GmbH & Co. KGaA, Weinheim

2365709x, 2020, 1, Downloaded from https://onlinelibrary.wiley.com/doi/10.1002/admt.201900800 by Sungkyunkwan University, Wiley Online Library on [14/04/2024]. See the Terms and Conditions (https://onlinelibrary.wiley.com/terms-and-conditions) on Wiley Online Library for rules of use; OA articles are governed by the applicable Creative Commons License

to the high capacitance of the interface. As a comparison, the optimized mean noise level of previously reported devices with capacitive coupling through t-SiO_2 falls into the range of 50–80 µV.[5,6] Figure 6D displays the statistics of signal-to-noise ratio with an average value of ≈48 dB.

3. Conclusion

In summary, the results presented here provide a materials and integration strategy for use of multilayer stacks of HfO_2, Au and a structure of p^{++}-Si//SiO_2 as a long-lived biofluid barrier and high quality capacitive sensing interface for flexible, active electronic bioimplants. Experimental and theoretical studies reveal that these capping multilayers on p^{++}-Si//t-SiO_2 dramatically reduce the rates of diffusion of water to the p^{++}-Si, thereby extending by an order of magnitude the lifetime of the bioimplants. Comparative evaluations highlight the advantages in scaling to high-density, high-resolution arrays with an extended lifetime of about one order of magnitude at physiological temperature compared to the case without coating layers. These findings suggest a promising pathway toward high-resolution neural interfaces with levels of flexibility, recording fidelity, and longevity that can address a wide range of applications in biomedical research and clinical practice.

4. Experimental Section

Fabrication of Transistor Arrays: The fabrication of the transistors began with cleaning of the SOI substrates (200 nm device-grade Si, 1 µm t-SiO_2, and 200 µm Si handle wafer). Photolithographic patterning, deposition, and etching formed boron (p-type) and phosphorus (n-type) doped Si NMs as the conductive sensing pathways and NMOS backplane, respectively. Thermal oxidation and ALD formed ≈50 nm thick layers of t-SiO_2 and ≈13 nm thick layers of Al_2O_3 as the gate stack. Photolithographic patterning and immersion in buffered oxide etchant (BOE) opened contact areas to the Si, followed by deposition and patterning of bilayers of Cr (10 nm) and Au (300 nm) as the metal interconnects and source, drain, and gate electrodes. An additional metal contact established electrical interconnects between the p^{++}-Si regions and the channels of the transistors. Spin coating layer of PI (1.5 µm) followed by curing in a vacuum oven formed uniform overcoat. Deposition of a 20 nm thick film of Al_2O_3 on the PI by ALD yielded an adhesion layer for bonding. Separately, a glass slide served as a temporary substrate support for a spin-cast layer of polydimethylsiloxane (PDMS), a Kapton film (12 µm), and a thin film of ALD-Al_2O_3 (20 nm). A commercial adhesive (Kwik-Sil, World Precision Instruments) facilitated bonding between the surface of the device and material stack on the handling substrate (pressure: 50 kPa). Inductively coupled plasma (ICP) RIE with SF_4 and O_2 removed the Si handle wafer and exposed the buried t-SiO_2. Photolithographic patterning followed by combined dry (CF_4/O_2) and wet (BOE) etching opened selective regions aligned to the p^{++}-Si as the conductive via. Thermal evaporation of 10 nm Cr/300 nm Au, photolithography, and metal etching yielded metal pads on the top to define the sensing areas. Additional steps using ALD formed a conformal coating of ≈50 nm HfO_2 (100–120 °C) as the final top layer. Tetrakis(dimethylamido)hafnium(IV) and H_2O served as the precursors. Covering the electrical contact area with Kapton tape before ALD minimized the growth of HfO_2 on the terminal pads for subsequent removal steps. Carefully peeling off the tape followed by photolithography, dry (ICP-RIE with SF_6 and O_2) and wet etching (BOE) opened contact areas for electrical measurement. Cutting the device with a razor blade and peeling the device off completed the fabrication steps. A probe station measured the electrical properties of the MOSFETs. In vitro assessments of multiplexed Si transistor arrays used a customized data acquisition system reported in refs. [5] and [6].

Soak Tests for Passive and Active Devices: A well structure formed in PDMS confined PBS over the target area of the device. Ultraviolet ozone treatment enhanced the adhesion between PDMS and the surface of the sample. For active devices, metal traces formed by electron-beam evaporation connected the active area to contact pads outside of the well for measurement and evaluation.

Supporting Information

Supporting Information is available from the Wiley Online Library or from the author.

Acknowledgements

J.L., R.L., and C.-H.C. contributed equally to this work. This work was supported by the Center for Bio-Integrated Electronics at Northwestern University. The authors acknowledge the use of facilities in the Micro and Nanotechnology Laboratory and the Frederick Seitz Materials Research Laboratory for Advanced Science and Technology at the University of Illinois at Urbana-Champaign, and the Northwestern University's Atomic and Nanoscale Characterization Experimental Center (NUANCE). J.L. Acknowledges the support from the startup funds of The Ohio State University. R.L. acknowledges the support from the National Natural Science Foundation of China (11972103), LiaoNing Revitalization Talents Program (XLYC1807126), and Fundamental Research Funds for the Central Universities of China (DUT18GF101). C.-H.C. and J.V. acknowledge support from the National Institutes of Health (U01-NS099697). K.J.Y. acknowledges the support from the National Research Foundation of Korea (NRF-2019R1A2C2086085 and NRF-2018M3A7B4071109).

Conflict of Interest

The authors declare no conflict of interest.

Keywords

biofluid barriers, biointegrated electronics, high-κ dielectrics, neural interfaces

Received: September 11, 2019
Revised: October 26, 2019
Published online: November 29, 2019

[1] B. Litt, R. Esteller, J. Echauz, M. D'Alessandro, R. Shor, T. Henry, P. Pennell, C. Epstein, R. Bakay, M. Dichter, G. Vachtsevanos, *Neuron* **2001**, *30*, 51.
[2] A. Canales, X. T. Jia, U. P. Froriep, R. A. Koppes, C. M. Tringides, J. Selvidge, C. Lu, C. Hou, L. Wei, Y. Fink, P. Anikeeva, *Nat. Biotechnol.* **2015**, *33*, 277.
[3] K. L. Montgomery, A. J. Yeh, J. S. Ho, V. Tsao, S. M. Iyer, L. Grosenick, E. A. Ferenczi, Y. Tanabe, K. Deisseroth, S. L. Delp, A. S. Y. Poon, *Nat. Methods* **2015**, *12*, 969.
[4] J. Viventi, D. H. Kim, L. Vigeland, E. S. Frechette, J. A. Blanco, Y. S. Kim, A. E. Avrin, V. R. Tiruvadi, S. W. Hwang, A. C. Vanleer, D. F. Wulsin, K. Davis, C. E. Gelber, L. Palmer, J. Van der Spiegel,

 © 2019 WILEY-VCH Verlag GmbH & Co. KGaA, Weinheim

2365709x, 2020, 1, Downloaded from https://onlinelibrary.wiley.com/doi/10.1002/admt.201900800 by Sungkyunkwan University, Wiley Online Library on [14/04/2024]. See the Terms and Conditions (https://onlinelibrary.wiley.com/terms-and-conditions) on Wiley Online Library for rules of use; OA articles are governed by the applicable Creative Commons License

J. Wu, J. L. Xiao, Y. G. Huang, D. Contreras, J. A. Rogers, B. Litt, *Nat. Neurosci.* **2011**, *14*, 1599.
[5] H. Fang, K. J. Yu, C. Gloschat, Z. J. Yang, E. M. Song, C. H. Chiang, J. N. Zhao, S. M. Won, S. Y. Xu, M. Trumpis, Y. D. Zhong, S. W. Han, Y. G. Xue, D. Xu, S. W. Choi, G. Cauwenberghs, M. Kay, Y. G. Huang, J. Viventi, I. R. Efimov, J. A. Rogers, *Nat. Biomed. Eng.* **2017**, *1*, 0038.
[6] H. Fang, J. N. Zhao, K. J. Yu, E. M. Song, A. B. Farimani, C. H. Chiang, X. Jin, Y. G. Xue, D. Xu, W. B. Du, K. J. Seo, Y. D. Zhong, Z. J. Yang, S. M. Won, G. H. Fang, S. W. Choi, S. Chaudhuri, Y. G. Huang, M. A. Alam, J. Viventi, N. R. Aluru, J. A. Rogers, *Proc. Natl. Acad. Sci. U. S. A.* **2016**, *113*, 11682.
[7] J. Viventi, D. H. Kim, J. D. Moss, Y. S. Kim, J. A. Blanco, N. Annetta, A. Hicks, J. L. Xiao, Y. G. Huang, D. J. Callans, J. A. Rogers, B. Litt, *Sci. Transl. Med.* **2010**, *2*, 24ra22.
[8] M. A. Escabi, H. L. Read, J. Viventi, D. H. Kim, N. C. Higgins, D. A. Storace, A. S. K. Liu, A. M. Gifford, J. F. Burke, M. Campisi, Y. S. Kim, A. E. Avrin, J. Van der Spiegel, Y. G. Huang, M. Li, J. Wu, J. A. Rogers, B. Litt, Y. E. Cohen, *J. Neurophysiol.* **2014**, *112*, 1566.
[9] T. Someya, Y. Kato, T. Sekitani, S. Iba, Y. Noguchi, Y. Murase, H. Kawaguchi, T. Sakurai, *Proc. Natl. Acad. Sci. U. S. A.* **2005**, *102*, 12321.
[10] G. T. Hwang, D. Im, S. E. Lee, J. Lee, M. Koo, S. Y. Park, S. Kim, K. Yang, S. J. Kim, K. Lee, K. J. Lee, *ACS Nano* **2013**, *7*, 4545.
[11] M. H. Park, J. Y. Kim, T. H. Han, T. S. Kim, H. Kim, T. W. Lee, *Adv. Mater.* **2015**, *27*, 4308.
[12] N. T. Kalyani, S. J. Dhoble, *Renewable Sustainable Energy Rev.* **2015**, *44*, 319.
[13] X. Z. Xie, L. Rieth, S. Merugu, P. Tathireddy, F. Solzbacher, *Appl. Phys. Lett.* **2012**, *101*, 09370.
[14] J. Ahmad, K. Bazaka, L. J. Anderson, R. D. White, M. V. Jacob, *Renewable Sustainable Energy Rev.* **2013**, *27*, 104.
[15] M. C. Choi, Y. Kim, C. S. Ha, *Prog. Polym. Sci.* **2008**, *33*, 581.
[16] T. N. Chen, D. S. Wuu, C. C. Wu, C. C. Chiang, Y. P. Chen, R. H. Horng, *Plasma Processes Polym.* **2007**, *4*, 180.
[17] M. D. Groner, S. M. George, R. S. McLean, P. F. Carcia, *Appl. Phys. Lett.* **2006**, *88*, 051907.
[18] D. Yu, Y. Q. Yang, Z. Chen, Y. Tao, Y. F. Liu, *Opt. Commun.* **2016**, *362*, 43.
[19] J. Jeong, F. Laiwalla, J. Lee, R. Ritasalo, M. Pudas, L. Larson, V. Leung, A. Nurmikko, *Adv. Funct. Mater.* **2019**, *29*, 1806440.
[20] P. J. Rousche, R. A. Normann, *J. Neurosci. Methods* **1998**, *82*, 1.
[21] R. R. Harrison, P. T. Watkins, R. J. Kier, R. O. Lovejoy, D. J. Black, B. Greger, F. Solzbacher, *IEEE J. Solid-State Circuits* **2007**, *42*, 123.
[22] A. C. Hoogerwerf, K. D. Wise, *IEEE Trans. Biomed. Eng.* **1994**, *41*, 1136.
[23] K. D. Wise, D. J. Anderson, J. F. Hetke, D. R. Kipke, K. Najafi, *Proc. IEEE* **2004**, *92*, 76.
[24] R. S. Sanders, M. T. Lee, *Proc. IEEE* **1996**, *84*, 480.
[25] H. S. Mayberg, A. M. Lozano, V. Voon, H. E. McNeely, D. Seminowicz, C. Hamani, J. M. Schwalb, S. H. Kennedy, *Neuron* **2005**, *45*, 651.
[26] L. Bowman, J. D. Meindl, *IEEE Trans. Biomed. Eng.* **1986**, *BME-33*, 248.
[27] J. H. Li, E. M. Song, C. H. Chiang, K. J. Yu, J. Koo, H. N. Du, Y. S. Zhong, M. Hill, C. Wang, J. Z. Zhang, Y. S. Chen, L. M. Tian, Y. D. Zhong, G. H. Fang, J. Viventi, J. A. Rogers, *Proc. Natl. Acad. Sci. U. S. A.* **2018**, *115*, E9542.
[28] Y. K. Lee, K. J. Yu, E. M. Song, A. B. Farimani, F. Vitale, Z. Q. Xie, Y. Yoon, Y. Kim, A. Richardson, H. W. Luan, Y. X. Wu, X. Xie, T. H. Lucas, K. Crawford, Y. F. Mei, X. Feng, Y. G. Huang, B. Litt, N. R. Aluru, L. Yin, J. A. Rogers, *ACS Nano* **2017**, *11*, 12562.
[29] Y. K. Lee, K. J. Yu, Y. Kim, Y. Yoon, Z. Q. Xie, E. M. Song, H. W. Luan, X. Feng, Y. G. Huang, J. A. Rogers, *ACS Appl. Mater. Interfaces* **2017**, *9*, 42633.
[30] J. H. Li, R. Li, H. N. Du, Y. S. Zhong, Y. S. Chen, K. W. Nan, S. M. Won, J. Z. Zhang, Y. G. Huang, J. A. Rogers, *ACS Nano* **2019**, *13*, 660.
[31] X. Feng, S. R. Dong, H. Wong, D. Q. Yu, K. L. Pey, K. Shubhakar, W. S. Lau, *Microelectron. Reliab.* **2016**, *61*, 78.
[32] Y. W. Lu, J. Shieh, F. Y. Tsai, *Acta Mater.* **2016**, *115*, 68.
[33] F. J. Ramos, T. Maindron, S. Bechu, A. Rebai, M. Fregnaux, M. Bouttemy, J. Rousset, P. Schulz, N. Schneider, *Sustainable Energy Fuels* **2018**, *2*, 2468.
[34] J. Rhie, D. Lee, Y. M. Bahk, J. Jeong, G. Choi, Y. Lee, S. Kim, S. Hong, D. S. Kim, *J. Micro Nanolithogr. MEMS MOEMS* **2018**, *17*, 023504.
[35] R. Yang, H. T. Li, K. K. H. Smithe, T. R. Kim, K. Okabe, E. Pop, J. A. Fan, H. S. P. Wong, *Nat. Electron.* **2019**, *2*, 108.
[36] L. Wu, H. X. Liu, J. B. Li, S. L. Wang, X. Wang, *Nanoscale Res. Lett.* **2019**, *14*, 177.
[37] A. S. Sokolov, Y. R. Jeon, S. Kim, B. Ku, D. Lim, H. Han, M. G. Chae, J. Lee, B. G. Ha, C. Choi, *Appl. Surf. Sci.* **2018**, *434*, 822.
[38] Y. L. Chueh, C. N. Boswell, C. W. Yuan, S. J. Shin, K. Takei, J. C. Ho, H. Ko, Z. Y. Fan, E. E. Haller, D. C. Chrzan, A. Javey, *Nano Lett.* **2010**, *10*, 393.
[39] M. M. Xiao, C. G. Qiu, Z. Y. Zhang, L. M. Peng, *ACS Appl. Mater. Interfaces* **2017**, *9*, 34050.
[40] M. Thammasack, G. De Micheli, P. E. Gaillardon, *J. Electroceram.* **2017**, *39*, 137.
[41] D. E. King, *J. Vac. Sci. Technol., A* **1995**, *13*, 1247.
[42] P. Ganesh, P. R. C. Kent, G. M. Veith, *J. Phys. Chem. Lett.* **2011**, *2*, 2918.
[43] Z. Wu, Z. Jiang, Y. Jin, F. Xiong, W. Huang, *J. Phys. Chem. C* **2014**, *118*, 26258.
[44] F. Xu, I. Fampiou, C. R. O'Connor, S. Karakalos, F. Hiebel, E. Kaxiras, R. J. Madix, C. M. Friend, *Phys. Chem. Chem. Phys.* **2018**, *20*, 2196.
[45] M. S. Ide, R. J. Davis, *Acc. Chem. Res.* **2014**, *47*, 825.
[46] J. Yota, *ECS Trans.* **2013**, *53*, 281.
[47] E. K. Seo, J. W. Lee, H. M. Sung-Suh, M. M. Sung, *Chem. Mater.* **2004**, *16*, 1878.
[48] H. Moshe, G. Levi, D. Sharon, Y. Mastai, *Surf. Sci.* **2014**, *629*, 88.
[49] L. Newton, T. Slater, N. Clark, A. Vijayaraghavan, *J. Mater. Chem. C* **2013**, *1*, 376.
[50] R. Li, H. T. Cheng, Y. W. Su, S. W. Hwang, L. Yin, H. Tao, M. A. Brenckle, D. H. Kim, F. G. Omenetto, J. A. Rogers, Y. G. Huang, *Adv. Funct. Mater.* **2013**, *23*, 3106.
[51] P. V. Danckwerts, *Trans. Faraday Soc.* **1950**, *46*, 300.

© 2019 WILEY-VCH Verlag GmbH & Co. KGaA, Weinheim

2365709x, 2020, 1, Downloaded from https://onlinelibrary.wiley.com/doi/10.1002/admt.201900800 by Sungkyunkwan University, Wiley Online Library on [14/04/2024]. See the Terms and Conditions (https://onlinelibrary.wiley.com/terms-and-conditions) on Wiley Online Library for rules of use; OA articles are governed by the applicable Creative Commons License